

# Angular distributions for the inelastic scattering of $\text{NO}(X^2\Pi)$ with $\text{O}_2(X^3\Sigma_g^-)$

M. Brouard, S. D. S. Gordon, B. Nichols, E. Squires, V. Walpole, F. J. Aoiz, and S. Stolte

Citation: *The Journal of Chemical Physics* **146**, 204304 (2017); doi: 10.1063/1.4983706

View online: <https://doi.org/10.1063/1.4983706>

View Table of Contents: <http://aip.scitation.org/toc/jcp/146/20>

Published by the [American Institute of Physics](#)

---

## Articles you may be interested in

[Integral steric asymmetry in the inelastic scattering of  \$\text{NO}\(X^2\Pi\)\$](#)

*The Journal of Chemical Physics* **146**, 014302 (2017); 10.1063/1.4972565

[Stereodynamics in  \$\text{NO}\(X\) + \text{Ar}\$  inelastic collisions](#)

*The Journal of Chemical Physics* **144**, 224301 (2016); 10.1063/1.4952649

[Pair-correlated stereodynamics for diatom-diatom rotational energy transfer:  \$\text{NO}\(A^2\Sigma^+\) + \text{N}\_2\$](#)

*The Journal of Chemical Physics* **147**, 013912 (2017); 10.1063/1.4979487

[Perspective: Advanced particle imaging](#)

*The Journal of Chemical Physics* **147**, 013601 (2017); 10.1063/1.4983623

[Velocity map imaging of ions and electrons using electrostatic lenses: Application in photoelectron and photofragment ion imaging of molecular oxygen](#)

*Review of Scientific Instruments* **68**, 3477 (1997); 10.1063/1.1148310

[Imaging diffraction oscillations for inelastic collisions of NO radicals with He and  \$\text{D}\_2\$](#)

*The Journal of Chemical Physics* **147**, 013918 (2017); 10.1063/1.4981023

---

PHYSICS TODAY

WHITEPAPERS

### ADVANCED LIGHT CURE ADHESIVES

Take a closer look at what these environmentally friendly adhesive systems can do

READ NOW

PRESENTED BY  
**MASTERBOND**  
ADHESIVES | SEALANTS | COATINGS

# Angular distributions for the inelastic scattering of NO( $X^2\Pi$ ) with O<sub>2</sub>( $X^3\Sigma_g^-$ )

M. Brouard,<sup>1,a)</sup> S. D. S. Gordon,<sup>1</sup> B. Nichols,<sup>1</sup> E. Squires,<sup>1</sup> V. Walpole,<sup>1</sup> F. J. Aoiz,<sup>2,b)</sup> and S. Stolte<sup>3,c),d)</sup>

<sup>1</sup>The Department of Chemistry, The Chemical Research Laboratory, University of Oxford, 12 Mansfield Road, Oxford OX1 3TA, United Kingdom

<sup>2</sup>Departamento de Química Física, Facultad de Química, Universidad Complutense, 28040 Madrid, Spain

<sup>3</sup>The Jilin Institute of Atomic and Molecular Physics, Qianjin Avenue, Changchun 130012, China

(Received 14 January 2017; accepted 25 April 2017; published online 30 May 2017)

The inelastic scattering of NO( $X^2\Pi$ ) by O<sub>2</sub>( $X^3\Sigma_g^-$ ) was studied at a mean collision energy of 550 cm<sup>-1</sup> using velocity-map ion imaging. The initial quantum state of the NO( $X^2\Pi$ ,  $v = 0$ ,  $j = 0.5$ ,  $\Omega = 0.5$ ,  $\epsilon = -1$ ,  $f$ ) molecule was selected using a hexapole electric field, and specific  $\Lambda$ -doublet levels of scattered NO were probed using (1 + 1') resonantly enhanced multiphoton ionization. A modified “onion-peeling” algorithm was employed to extract angular scattering information from the series of “pancaked,” nested Newton spheres arising as a consequence of the rotational excitation of the molecular oxygen collision partner. The extracted differential cross sections for NO( $X$ )  $f \rightarrow f$  and  $f \rightarrow e$   $\Lambda$ -doublet resolved, spin-orbit conserving transitions, partially resolved in the oxygen co-product rotational quantum state, are reported, along with O<sub>2</sub> fragment pair-correlated rotational state population. The inelastic scattering of NO with O<sub>2</sub> is shown to share many similarities with the scattering of NO( $X$ ) with the rare gases. However, subtle differences in the angular distributions between the two collision partners are observed. *Published by AIP Publishing.* [<http://dx.doi.org/10.1063/1.4983706>]

## I. INTRODUCTION

Crossed molecular beam experiments provide a direct means to understand the forces in operation when molecules approach and collide with one another. In combination with velocity-map ion imaging techniques, crossed molecular beam experiments can be used to obtain angular scattering distributions, which are proportional to the differential cross section (DCS) and quantify the  $\mathbf{k}\text{-}\mathbf{k}'$  vector correlation. Over the last few decades, a significant amount of work has been done to understand the role of attractive and repulsive forces, and quantum scattering effects, in encounters between NO( $X$ ) and the rare gases.<sup>1–16</sup> Recent experiments have highlighted that exact quantum scattering calculations can reproduce fine details of the experimental images, for a variety of vector correlations.<sup>14–24</sup>

The lessons learned in the scattering of NO( $X$ ) with atomic species, such as the rare gases, can be applied to more complicated systems, with many more degrees of freedom. The next step-up in complexity from the diatom-atom system is the diatom-diatom case, potentially leading to inelastic scattering in which both collision partners may be rotationally excited. This adds considerable complexity to both the experimental and theoretical probing of the underlying potential energy surface (PES). Typically, studies on these inelastic collisions have

focused on systems in which only a single molecule is open shell in nature, for example, O<sub>2</sub> + H<sub>2</sub> or OH + HX, since there are no spin-coupling effects with the closed-shell partner, and the number of PESs required to describe the system is limited.<sup>25–31</sup> In systems which include two open shell species, such as NO + O<sub>2</sub> and NO + OH,<sup>27</sup> coupling between the spins of the two molecules must be considered, increasing the complexity of the system considerably. Whilst the scattering of NO with oxygen has previously been investigated,<sup>30,31</sup> the focus was largely on determining final rotational population distributions and NO( $X$ )  $\Lambda$ -doublet population ratios. Furthermore, these studies were not able to select the initial  $\Lambda$ -doublet level of the NO molecule. Here, we present angular distributions obtained for the scattering of NO( $X$ ), initially state-selected in the  $|v = 0, j = 0.5, \Omega = 0.5, \epsilon = -1, f\rangle$   $\Lambda$ -doublet level, with O<sub>2</sub>( $X$ ), a system whose dynamics, in principle, could take place on four coupled PESs.

The experimental detection method used in the current work is that of velocity-map<sup>32</sup> ion imaging.<sup>33</sup> For diatom-diatom scattering, the rotational excitation induced in both collision partners also leads to increased complexity in the ion image analysis. Within each ion image, for a single probed NO quantum state, there are potentially multiple rings observed due to the presence of many different occupied rotational states of the O<sub>2</sub> collision partner. Each of these rings, an effective ion image for each ( $j'_{\text{NO}}, N'_{\text{O}_2}$ ) fragment pair, must be analysed separately to obtain the full  $\mathbf{k}\text{-}\mathbf{k}'$  correlation for the system. (Here  $N'_{\text{O}_2}$  is the total O<sub>2</sub> angular momentum apart from the spin, whilst  $j'_{\text{NO}}$  is the NO total rotational momentum excluding the nuclear spin.) There are currently many methods available for the analysis of multiple nested rings within an ion image, arising from several different nested “pancaked” Newton spheres,

<sup>a)</sup>Electronic mail: mark.brouard@chem.ox.ac.uk

<sup>b)</sup>Electronic mail: aoiz@quim.ucm.es

<sup>c)</sup>Electronic mail: stolte@chem.vu.nl

<sup>d)</sup>Also affiliated with: Department of Physics and Astronomy, LaserLaB, Vrije Universiteit, Amsterdam, De Boelelaan 1081, 1081 HV Amsterdam, The Netherlands and Laboratoire Francis Perrin, Bâtiment 522, DRECEM/SPAM/CEA Saclay, 91191 Gif sur Yvette, France.

including Abel-inversion,<sup>34–38</sup> “onion-peeling,”<sup>39,40</sup> and numerical methods<sup>41–44</sup> such as entropic analysis and forward convolution. These methods have typically been used for photofragment imaging,<sup>34,35,37,39,43,45</sup> in which multiple product velocities must be measured in the same experiment. This is similar to the requirements for diatom-diatom scattering, in which the state-selected scattered NO molecule has a different outgoing velocity depending on the  $N'_{O_2}$  co-product rotational state. However, each of these methods has its own strengths and weaknesses. For both Abel-inversion and onion-peeling algorithms, ion images are typically required to be cylindrically symmetric, whilst numerical methods are typically not constrained by such symmetry requirements.

Slice imaging,<sup>46–55</sup> in which one or more time slices through the Newton sphere are extracted as separate ion images, would be an ideal method to extract DCSs for the different oxygen rotational states from the overall ion image. Slice imaging would allow the extraction of the central slice of the Newton sphere, removing out-of-plane scattering contributions from the ion image and thus more directly yielding the velocity distribution of the probed scattered product. Unfortunately, such a method is currently challenging to be implemented in the current experiment due to the modest kinetic energy release of the NO scattered product and the signal reduction arising upon slicing of the ion image. Therefore, in the present work, we use a modified version of the onion-peeling algorithm to extract information from the experimental “pancaked” ion images, which accommodates the non-cylindrically symmetric ion images observed in the present experimental configuration. A further advantage of the method employed is that it does not produce noise-dependent artefacts during the analysis process, a problem frequently encountered with Abel-inversion methods.<sup>36–38</sup>

This paper is laid out as follows: Section II describes the electronic structure of the diatom-diatom system and the potential energy surface for such a collision. The experimental and computational details are summarized in Sec. III, which includes a detailed description of the analysis of experimental images via a modified onion-peeling algorithm. Differential cross sections and state-resolved population for NO + O<sub>2</sub> scattering are presented in Sec. IV, together with a comparison between the diatomic oxygen collision partner and atomic argon. Conclusions and the outlook for the future then follow in Sec. V.

## II. ELECTRONIC STRUCTURE AND SURFACES

The complexity of the PESs upon which scattering occurs is determined by the electronic structure of the NO–O<sub>2</sub> system. NO(X) has a single electron in a  $\pi^*$  orbital, leading to a  $^2\Pi$  ground state term, whilst O<sub>2</sub> has two electrons in its corresponding  $\pi_g^*$  orbital, giving rise to a ground  $^3\Sigma_g^-$  term. The ground electronic state of NO is split into two spin-orbit states, with the ground  $\Omega = 1/2$  and excited  $3/2$  spin-orbit states separated by 123 cm<sup>−1</sup>. Each NO rotational state is split further into two near degenerate  $\Lambda$ -doublet levels, which are symmetric ( $\epsilon = +1, e$ ) and antisymmetric ( $\epsilon = -1, f$ ) combinations of the  $+\Omega$  and  $-\Omega$  wavefunctions and which differ in parity, given by  $p = \epsilon(-1)^{j-1/2}$ . Each rotational level of the ground state

of O<sub>2</sub>, on the other hand, is split into three spin-rotation states ( $j = N + 1, N$ , and  $N - 1$ , i.e., for  $N = 1, j = 2, 1$ , and  $0$ , respectively). With the approach of NO and O<sub>2</sub> in planar configurations, the interaction of the two diatomics gives rise to four PESs of  $^2A'$ ,  $^2A''$ ,  $^4A'$ , and  $^4A''$  symmetry. An accurate *ab initio* calculation of these surfaces, and of the couplings between them, is particularly difficult, and distinguishing the energies of each surface is complicated. Furthermore, exact quantum dynamics calculations would, in principle, have to be performed on the four coupled PESs, making the coupled equations extremely difficult to solve.

Since the ground state of O<sub>2</sub> is a  $^3\Sigma_g^-$  state, and oxygen has zero nuclear spin, only rotational states corresponding to antisymmetric rotational wavefunctions exist and hence can be populated before and after collision. Oxygen therefore can only be rotationally excited to odd  $N'_{O_2}$  levels, with the ground state  $N_{O_2} = 1$  being the most populated level initially in a cold molecular beam. Whilst oxygen is a somewhat more complex collision partner than the rare gases, the diatom does share some similarities with argon, despite being a radical, due to its symmetry and lack of dipole moment (although, unlike the rare gases, it does possess a quadrupole moment). This facilitates comparisons with quantum mechanical calculations and experimental data for the inelastic scattering of NO by Ar.

In the case of NO + Ar, with the nonlinear approach of the atom and molecule, the degeneracy of the  $^2\Pi$  state is lifted, resulting in two potential energy surfaces of  $A'$  and  $A''$  symmetry. In the case of Hund’s case (a) molecules, it has been shown<sup>56,57</sup> that the spin-orbit conserving transitions can be considered to take place on a summed potential

$$V_{\text{sum}}(R, \gamma) = \frac{1}{2}[V_{A'}(R, \gamma) + V_{A''}(R, \gamma)], \quad (1)$$

while spin-orbit changing collisions are coupled by a difference potential

$$V_{\text{diff}}(R, \gamma) = \frac{1}{2}[V_{A''}(R, \gamma) - V_{A'}(R, \gamma)]. \quad (2)$$

Here,  $V_{A'}$  and  $V_{A''}$  are the potential energy surfaces (PESs) for the two lowest lying electronic states of NO(X) + Ar,  $R$  is the distance between the Ar atom and the centre of mass of the diatom, and  $\gamma$  is the angle between  $\mathbf{R}$  and the NO bond axis,  $\mathbf{r}$ . In the case of NO(X) + O<sub>2</sub>, a similar description might be anticipated, but now involving both doublet and quartet  $V_{\text{sum}}(R, \gamma)$  and  $V_{\text{diff}}(R, \gamma)$  potentials, with possible additional spin-orbit coupling between the states of differing multiplicities. It is worth noting, however, that since oxygen is a Hund’s case (b) molecule, this relationship may be less strict for scattering with molecular oxygen compared to that with a rare gas atom.

Although accurate PESs are currently unavailable for the NO + O<sub>2</sub> system, it has been speculated previously that the collisions between NO and O<sub>2</sub> should have a deep attractive well, due to the spin-pairing of the collision partners.<sup>30</sup> One might expect the presence of such deep potential energy wells to be manifested as  $\ell$ -type rainbows in the differential cross sections for low rotational excitation.<sup>4,8,13–16</sup> Because NO and O<sub>2</sub> are fairly light systems, and given that spin-orbit coupling is

negligible in Hund's case (b), it might be expected that spin-orbit coupling will be relatively small and that the aforementioned mixing between the doublet ( $^2A$ ) and quartet ( $^4A$ ) surfaces is not likely to be significant.<sup>58</sup> The doublet and quartet PESs may reasonably be expected to be accessed approximately according to their spin degeneracy, as such scattering on the quartet surfaces would be expected to be roughly twice as important as scattering on the doublet surfaces. Interestingly, the path of the two diatoms over the PESs can, in principle, lead to the formation of the energized  $\text{NO}_3$  radical species.<sup>30,59–61</sup> However, the energy barrier to reaching this region of the PES is expected to be very high ( $\approx 16\,000\text{ cm}^{-1}$ )<sup>60,61</sup> and is thus not accessible at the collision energy of the current experiment ( $E_{\text{coll}} = 550\text{ cm}^{-1}$ ).

### III. METHODS

#### A. Experiment

The experimental apparatus has been described in detail elsewhere and so is only summarized here.<sup>6,7,9,62,63</sup> The experiment consisted of a crossed molecular beam apparatus, coupled with velocity-map<sup>32</sup> ion imaging.<sup>33</sup> A pulsed general valve operating at 10 Hz allowed a mixture of 10% NO in Ar to pass into a source chamber, where it was cooled by supersonic expansion, skimmed (diameter 5 mm), and then collimated. The cooled NO(X) was then passed through a hexapole state-selector, held at  $\pm 10\text{ kV}$ , which exploited the Stark effect to focus a single  $\Lambda$ -doublet level of NO in the  $|v = 0, j = 0.5, \Omega = 0.5, \epsilon = -1, f\rangle$  quantum state into the interaction region. The state-selected NO(X) beam was then crossed at right angles with a beam of pure molecular oxygen, generated from a pulsed beam valve operated at 5 Hz. The  $\text{O}_2$  beam was cooled by supersonic expansion and singly skimmed (diameter 3 mm) before entering the interaction region. The  $\text{O}_2$  molecular beam temperature was probed by introducing a trace quantity of NO(X) into the oxygen molecular beam and recording the NO using  $(1 + 1')$  resonantly enhanced multiphoton ionization (REMPI) spectrum (see further below). The beam temperature,  $T_{\text{rot}} \sim 5\text{ K}$ , was sufficiently low that more than 93% of the  $\text{O}_2(\text{X})$  molecules in the molecular beam are in their lowest possible rotational quantum state,  $N_{\text{O}_2} = 1$ .

After collision between NO and  $\text{O}_2$ , the scattered NO(X) was ionized quantum state-selectively using  $(1 + 1')$  REMPI via the  $\text{NO } A \leftarrow X$  transition at wavelengths around 226 nm, with subsequent ionization at 308 nm. A photoelastic modulator (PEM) was used to select vertical (V) polarization of the 226 nm radiation (i.e., polarization parallel to the time-of-flight axis). The ionized NO products were then extracted by velocity-map ion imaging optics onto a two-dimensional imaging detector. The scattered images of NO were found to be insensitive to the backing pressure of the  $\text{O}_2$  molecular beam, within the range 0.5 bars (50 kPa) to 3.0 bars (300 kPa). The mean experimental collision energy was measured to be  $550\text{ cm}^{-1}$  ( $\approx 68\text{ meV}$ ), with a full-width-at-half-maximum of  $50\text{ cm}^{-1}$ .

Sample images for the inelastic scattering of NO(X) by Ar were used to calibrate the instrument function and determine the instrument resolution. The instrument resolution has

contributions from several factors, including the volume of the laser interaction region and the velocity spreads in the molecular beams. To minimize such blurring, the pulse widths of the molecular beams were kept as short as possible, and the probe laser interaction volume was reduced. Despite the constraints of finite instrument resolution, we show below that it was still possible to obtain experimental DCSs for the  $\text{NO} + \text{O}_2$  system, fully quantum state-resolved in NO and partially resolved in the rotational state of the  $\text{O}_2$  co-product, by careful analysis and account for the finite instrument resolution in the fitting procedure. It should be noted that in the current experiments the product velocity resolution is largely limited by the initial velocity spreads in the molecular beams and, to a lesser extent, by the use of crushed ion imaging, as opposed to sliced imaging.

#### B. Quantum mechanical scattering calculations

The  $\text{NO} + \text{O}_2$  image data were also compared with the results of close-coupled (CC) quantum mechanical (QM) scattering calculations, treating  $\text{O}_2$  as a structureless Ar atom, but with the mass of  $\text{O}_2$ . Similar calculations for  $\text{NO} + \text{Ar}$  have been shown previously to agree very well with the experimental data for that system.<sup>7,10,11,14–16,62</sup> The full non-adiabatic close-coupled calculations were carried out on the  $\text{NO} + \text{Ar}$   $V_{\text{sum}}(R, \gamma)$  and  $V_{\text{diff}}(R, \gamma)$  coupled-cluster singles, doubles, perturbative triples [CCSD(T)] PESs of Alexander,<sup>19</sup> using the Hibridon suite of codes,<sup>64</sup> with the mass of Ar replaced by that of  $\text{O}_2$ . The QM results were averaged over the collision energy distribution, with the QM calculations performed at six sample points across the energy distribution. Rotational levels up to  $j' = 20.5$ , both  $\Lambda$ -doublet levels ( $\epsilon = -1, +1$ ), and spin-orbit manifolds ( $\Omega = 0.5, 1.5$ ) were included in the scattering wavefunction. The maximum partial wave was set to  $J = 160.5$  in order to achieve convergence, which corresponds to a classical impact parameter of  $6.8\text{ \AA}$ .

#### C. Image analysis

The analysis of experimental velocity-map ion images for the scattering of two diatomics is complicated, compared to the analysis of an atom-diatom collision, by the pairwise correlations between the final rotational states of the two molecules involved, in this case  $(j'_{\text{NO}}, N'_{\text{O}_2})$ . Since both the NO and  $\text{O}_2$  molecules are able to undergo rotational excitation during the collision, the experimental image for a specific final rotational state of NO,  $j'_{\text{NO}}$ , which is state-selectively detected in the REMPI scheme, is a sum over all the rotational states of the oxygen co-product populated upon collision. Within the experimental image, this is observed as a series of concentric rings, corresponding to the different “pan-caked” Newton spheres for the scattered oxygen co-products in the different final  $N'_{\text{O}_2}$  rotational states. Recall that only odd rotational states of  $\text{O}_2$  are populated due to nuclear spin statistics.

The radial size of an NO ion image, corresponding to specific NO and  $\text{O}_2$  final rotational states, is proportional to the center-of-mass speed of the scattered NO,  $u'_{\text{NO}}$ . This decreases with increasing  $N'_{\text{O}_2}$  according to the kinetic energy available to



the NO molecule, after partitioning the initial collision energy,  $E_{\text{coll}}$ , into both NO and O<sub>2</sub> rotational excitation,

$$r \propto u'_{\text{NO}} = \frac{m_{\text{O}_2}}{m_{\text{O}_2} + m_{\text{NO}}} \sqrt{\frac{2E'_t}{\mu}}, \quad (3)$$

where  $E'_t = E_{\text{coll}} - \Delta E_{\text{rot}}$  is the product relative translational energy and is a function of both O<sub>2</sub> and NO rotational energies. The change in the rotational energy on collision,  $\Delta E_{\text{rot}} = E'_{\text{rot}} - E_{\text{rot}}$ , contains contributions from both NO and O<sub>2</sub>. However, given the initial NO quantum state-selection in the experiment, and the REMPI detection scheme employed, the rotational energy term involving NO is fully defined in the experiment. Furthermore, the initial rotational energy of the O<sub>2</sub> molecule is dominated by that of the initially populated rotational state of O<sub>2</sub> in the molecular beam, which as we have seen is mainly in  $j_{\text{O}_2} = 1$ . Therefore, in principle, the nested NO ion images, corresponding to different O<sub>2</sub> co-product final rotational states, may be analysed to yield DCSs for each fragment pair, specified by rotational states  $j'_{\text{NO}}$  and  $N'_{\text{O}_2}$ .

In practice, the difference in scattered NO velocity between the lowest rotational levels of oxygen ( $N'_{\text{O}_2} = 1 - 5$ ) is very small ( $\sim 40 \text{ cm}^{-1}$ , neglecting spin-rotation coupling), amounting to a few pixels on the imaging detector. This leads to the overlap of the respective pancaked Newton spheres. This is exacerbated by experimental blurring across several pixels in the image mentioned in Sec. III A. As already noted in Sec. III A, in the present experiments the blurring is dominated by the contributions from the spreads in the initial velocity distributions of the molecular beams. Due to the experimental resolution achieved in the NO + O<sub>2</sub> scattering experiments, the rings caused by different oxygen states are blurred together, leading to an ion image with a broad distribution of pancaked Newton sphere radii, rather than well separated concentric rings, as shown in the right panel of Fig. 1. (For comparison, the left panel of Fig. 1 provides a comparison with the image obtained for the inelastic scattering of NO + Ar into the same final NO quantum state, obtained under very similar experimental conditions.) This blurring, particularly for the lowest rotational levels of O<sub>2</sub>, increases the complexity of the image analysis method, since each radius in the ion image will have contributions from several overlapping

oxygen states. Thus, each state must be recovered sequentially to account for contributions from other  $N'_{\text{O}_2}$ , using a modified onion-peeling algorithm to extract the correlated DCSs. Such algorithms were introduced by Bordas *et al.*<sup>34</sup> to analyse the results of photoelectron images, which were then extended for the use of photofragment images by Manzhos and Loomis.<sup>39</sup> The method has now been used to analyse a wide range of different photofragment ion images; however, in all cases the methods rely on the cylindrical symmetry of the image.<sup>34,39,40,65</sup> The image analysis procedure described here follows a similar methodology, adapted to allow for the fact that the ion images in the scattering experiments do not possess cylindrical symmetry.<sup>7,62</sup>

The experimental images are not a true representation of the  $\mathbf{k}\text{-}\mathbf{k}'$  correlation, but rather they represent a convolution of the total DCS (i.e., the differential cross sections for each  $N'_{\text{O}_2}$ , weighted by their relative contribution) with an instrument-dependent function. This instrument function has multiple contributions, which have been described in detail previously.<sup>7,62</sup> The instrument function must be determined from separate experimental measurements on a benchmark system with an accurately known DCS, to allow the evaluation of system independent parameters (such as laser positions and widths within the scattering chamber). System dependent parameters, such as the molecular beam velocities, are calculated separately for the NO + O<sub>2</sub> system. In this case, the scattering of NO by Ar was used as the benchmark system, due to the plethora of data confirming the accuracy of experimental data in comparison to QM scattering theory.<sup>3,7,14,20,62,66</sup> The pixel-to-velocity ratio (a conversion factor specific to the experimental apparatus) was determined from the known NO + Ar collision energy and the observed NO image radius. It is important to emphasize that the instrument function must be calculated separately for each  $N'_{\text{O}_2}$ , as the flux-density correction depends on the laboratory (LAB) frame velocity of the outgoing products, which will differ for each O<sub>2</sub> rotational state.

Note that the instrument function also allows for the effects of rotational alignment of the scattered NO molecules, observed with vertically (V) polarized probe laser radiation, using a simple kinematic apse correction.<sup>7,62</sup> Data were also recorded and analysed for a small subset of states with

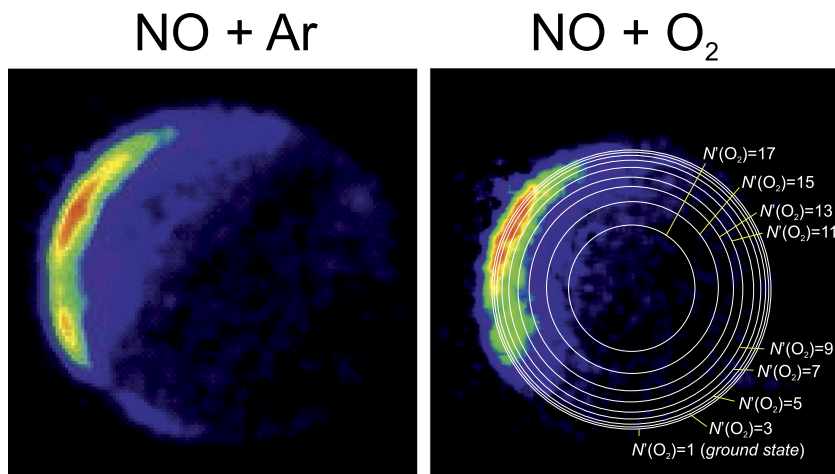


FIG. 1. Left panel: The experimental ion image for NO + Ar scattering into the  $j'_{\text{NO}} = 7.5e$ ,  $\Omega' = 0.5$  final state. Right panel: Comparison with experimental ion image for the scattering of NO + O<sub>2</sub> into the final state  $j'_{\text{NO}} = 7.5e$ ,  $\Omega' = 0.5$ . The panel also shows the radii of the Newton sphere for each final oxygen state,  $N'_{\text{O}_2}$ , convoluted within the image. Due to nuclear spin statistics only odd states may be populated, with  $N'_{\text{O}_2} = 1$  the ground state defining the outer radii of the image. The highest energetically accessible O<sub>2</sub> rotational quantum state in this case is  $N'_{\text{O}_2} = 17$ .

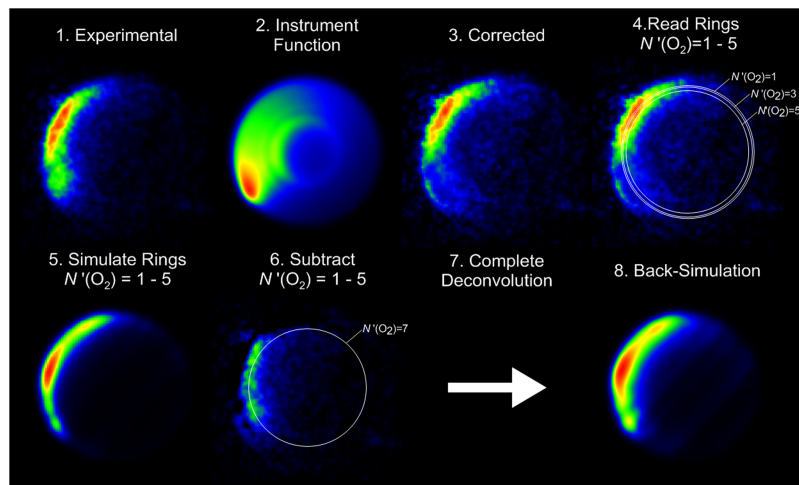


FIG. 2. Schematic showing the onion-peeling (deconvolution) methodology used to analyse the ion images recorded for the inelastic scattering of  $\text{NO} + \text{O}_2$ : the process is shown here for scattering into the  $|j'_{\text{NO}} = 7.5, \Omega' = 0.5, e' = 1, e\rangle$  state. The experimental image (panel 1) is flux density corrected (3) using the instrument function (2) for the specific experimental configuration. The lowest energy states are then extracted from the corrected image (4) by reading the radius equivalent to the Newton sphere for that specific  $(j'_{\text{NO}}, N'_{\text{O}_2})$  fragment pair. The outer rings of the image may then be simulated using the extracted DCSs (5) before they are unpeeled from the experimental image (6) by image subtraction. This process is repeated until the entire image has been “unpeeled.” The experimental ion image may be then back-simulated (8) from the extracted experimental DCS and  $\text{O}_2$  rotational population (7).

horizontally (H) polarised light. Within the combined errors of the extraction method, the angular distributions recovered from H and V polarised laser detection were found to be in very good agreement.

The onion-peeling method used to extract angular distributions and final  $\text{O}_2$  rotational state population is described pictorially in Fig. 2. The experimental image was initially “flux density corrected” by dividing the experimental image throughout by the simulated instrument function (for the specific  $N'_{\text{O}_2}$  of interest), where the latter function was calculated using parameters confirmed using recorded  $\text{NO} + \text{Ar}$

benchmark data (for system independent parameters) and the molecular beam velocities were calculated from the outer radius of the  $\text{NO} + \text{O}_2$  scattered ion images. The overlap between the instrument function and the experimental image was demonstrated by reading the radial intensity,  $I(r)$ , of both images. Overlaying the theoretical radii of the Newton spheres for each  $N'_{\text{O}_2}$  state with the experimental radial intensity allows the position of the  $\text{O}_2$  states, relative to the intensity in the image, to be observed (as shown in the top left panel of Fig. 3, for scattering into  $j'_{\text{NO}} = 7.5 e$ ). The angular distribution (which is proportional to the DCS) was read from the

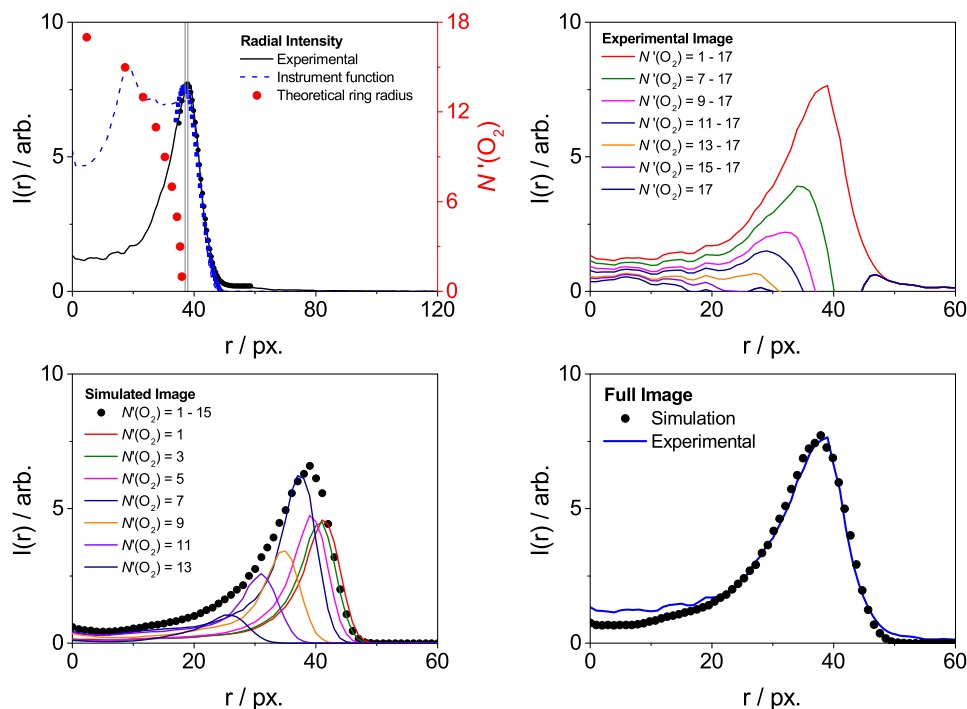


FIG. 3. Radial intensity,  $I(r)$ , plots for different stages of the analysis process, for the scattering of  $\text{NO}$  with  $\text{O}_2$  into  $j'_{\text{NO}} = 7.5 e$  on the spin-orbit conserving manifold. The top left panel shows the experimental (black line) and instrument function (blue dashed line) radial intensities fitted to a Gaussian peak (points in black and blue, respectively). The red points (and the red y-axis scale on the right of this panel) show the ring radii as a function of  $\text{O}_2$  rotational state, calculated in the absence of any blurring effects. The top of the Gaussian peak is taken to be the Newton sphere radius for the ground state,  $N'_{\text{O}_2} = 1$ . The grey vertical lines correspond to the radii between which the DCS of the ground state of  $\text{O}_2$  is read. The top right panel shows the experimental radial distributions after each deconvolution step; in which the full experimental image is shown by the red line. The bottom left panel shows the simulated radial distributions used to unpeel the image, whilst the bottom right panel shows the experimental distribution (blue line) compared to the rebuilt simulation (black points).

intensity of the image around a radius calculated according to Eq. (3). This accounted for the in-plane scattering of the product state in which  $O_2$  is formed with no rotational excitation, in coincidence with the  $j'_{NO}$  state of interest. The extracted angular distribution was then used to simulate the ion image for specific  $N'_{O_2}$ , using the instrument function parameters, the flux-density correction, and the polarisation parameters described above.<sup>7,10,62</sup> The contribution of the given  $O_2$  state was finally “peeled” from the raw experimental ion image by subtracting the appropriately weighted simulated image for the relevant  $N'_{O_2}$  from the experimental image. This resulted in a “new” experimental image, corresponding to higher  $O_2$  co-product rotational states, with any contributions from the lower  $N'_{O_2}$  state removed.

A new instrument function was then calculated for the next  $N'_{O_2}$  state, the “new” (subtracted) experimental image was then corrected with the new instrument function, and the angular distribution of the next oxygen rotational state was read from the experimental image. The ion image for the state was then simulated, weighted based upon the experimental image, and subtracted from the “new” (subtracted) experimental image. This process was continued until the signal-to-noise ratio became too low to allow the extraction of data, or until the energetic maximum populated  $O_2$  state,  $N'_{\max(O_2)}$ , was reached. Due to the very low scattering intensity in high  $N'_{O_2}$  states, the angular distributions for these states were not analysed for every  $j'_{NO}$ . The radial intensity from the experimental image after each subsequent subtraction is shown in the top right panel of Fig. 3, illustrating the removal of intensity in the experimental image as each state is unpeeled, with the radius of the resulting subtracted image becoming smaller as the  $O_2$  state of interest becomes higher. The intensity remaining on the outer edge of the initial experimental intensity arises from noise at the edge of the image as well as any effects from imperfections in the velocity mapping.

Because the difference between the lowest rotational states of oxygen ( $N'_{O_2} = 1, 3$ , and  $5$ ) is very small, typically corresponding to only a few pixels on the detector, and because each DCS was read over a 1 pixel wide bin, it was found necessary to read the DCS for each of these states in the same step. Thus, it was not possible to obtain distinct DCSs for  $N'_{O_2}$  in the

range 1–5, and only the average DCSs for these states were returned with confidence. For  $O_2$  states  $N'_{O_2} > 5$ , the energy difference (and hence radial difference on the detector) between adjacent  $O_2$  states was large enough to consider the contribution for each state separately. For transitions into  $j'_{NO} = 7.5e$ , the difference in rotational energy is approximately  $35\text{ cm}^{-1}$  for  $N'_{O_2} = 5 \rightarrow 7$  and  $46\text{ cm}^{-1}$  for  $N'_{O_2} = 7 \rightarrow 9$ .

Since the  $N'_{O_2}$  DCSs are extracted directly from the experimental image by the sequential removal of the intensity contributed by each oxygen state, population of each  $N'_{O_2}$  within the  $j'_{NO}$  state may be calculated by considering the integral of each state-resolved DCS. The complete back-simulated image may then be rebuilt from the simulations calculated for each  $N'_{O_2}$  state during the process, together with the associated  $O_2$  co-product rotational quantum state population. The bottom left panel of Fig. 3 shows the radial plots for each simulation once they have been appropriately weighted for the relative population in the system, showing the different contributions to the radial intensity for each state. The experimental radial intensity, bottom right panel of Fig. 3, is reproduced well by the summation of these weighted simulations.

The above methodology was tested on ion images recorded for the scattering of NO by Ar, in which only a single Newton sphere is present for each detected NO rotational state. Figure 4 shows the analysis for the scattering of NO and Ar into the  $j'_{NO} = 7.5e, \Omega' = 0.5$  quantum state. The same process is followed as for the case in which multiple Newton spheres are present: first, the theoretical radius of the image was calculated, and the DCS was extracted from the image, after suitable correction of the experimental image by dividing by the instrument function. This DCS obtained was then used to back-simulate an ion image. This was shown to be a good representation of the initial experimental image by using the subtraction method discussed above for  $O_2$  as the scattering partner. In the case of NO + Ar, because no other Newton spheres are present in the image after the subtraction of the simulated image, the resulting subtracted image should be effectively zero. Some signal is seen to remain due to noise from the background signal. The DCS resulting from the onion-peeling method is compared with that obtained from the fitting method described in detail previously by Eyles

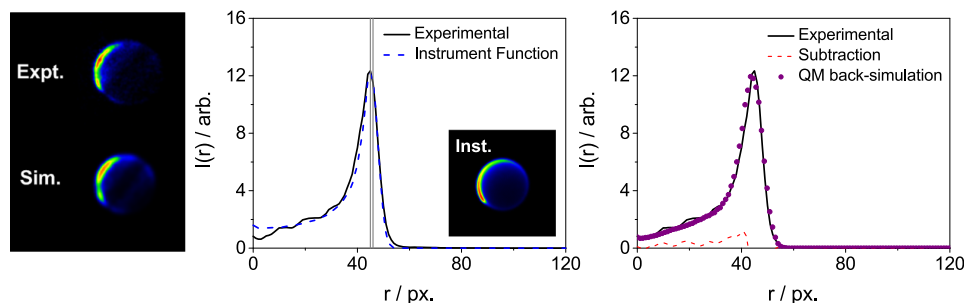


FIG. 4. Experimental and simulated ion images for NO ( $j' = 7.5e$ ) + Ar (left panel) and radial intensity,  $I(r)$ , plots (middle and right panels) for the different stages of the analysis process for the single Newton sphere formed from the scattering of NO + Ar into  $j' = 7.5e, \Omega' = 0.5$ . The middle panel shows the experimental (black line) and instrument function (blue dashed line) radial intensities. The grey vertical lines correspond to the radii (in pixels) between which the DCS of the state is read. The right panel shows the effect of using the deconvolution (onion-peeling) method for an atomic collision partner (which gives rise to a single Newton sphere): the simulation (purple circles), from the DCS extracted from the ion image, may be subtracted from the experimental radial intensity (black solid line) to effectively remove all intensity from the initial image. This process shows the principle for each ring within an ion image convoluted with several Newton spheres.

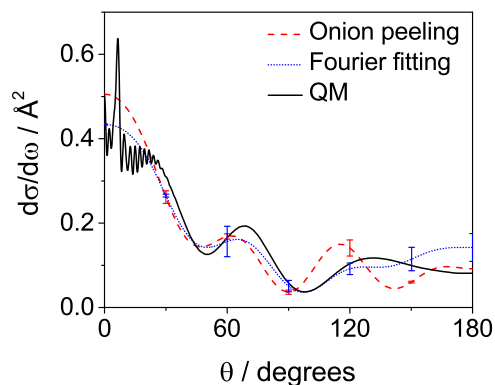


FIG. 5. DCSs for the scattering of NO + Ar into  $j' = 7.5e$ ,  $\Omega' = 0.5$ . The CC QM DCS, calculated using the correct Ar mass in this case, is shown with a continuous black line, the experimentally derived DCS obtained by fitting the images in Fourier space (denoted Fourier fitting)<sup>7,62</sup> is shown as a blue dotted line, and the DCS from the onion-peeling method is shown as a red dashed line. The QM data have been averaged over the experimental collision energy distribution. Error bars are calculated for the Fourier fitting by fitting the slow and fast sides of the image separately,<sup>7,62</sup> whilst error bars for the onion-peeling method are calculated using the slow and fast sides of the image, as well as fitting with a radius of  $\pm 1$  pixel.

*et al.*,<sup>62</sup> in Fig. 5, together with the DCS determined from CC QM calculations.<sup>7</sup> The onion-peeling method is shown to give good agreement with both the QM and fitted DCSs, apart from small differences in the backward scattered region, where the signal intensity is very low.

#### IV. RESULTS AND DISCUSSION

The experimental ion images for the inelastic scattering of NO with molecular oxygen, denoted by their respective  $j'_{\text{NO}}$ , are shown in Figs. 6 and 7 for spin-orbit conserving transitions into the final  $f$  and  $e$   $\Lambda$ -doublet levels, respectively. In both cases, the experimental ion image is shown on the top row, with the complete back-simulated image on the bottom row. In

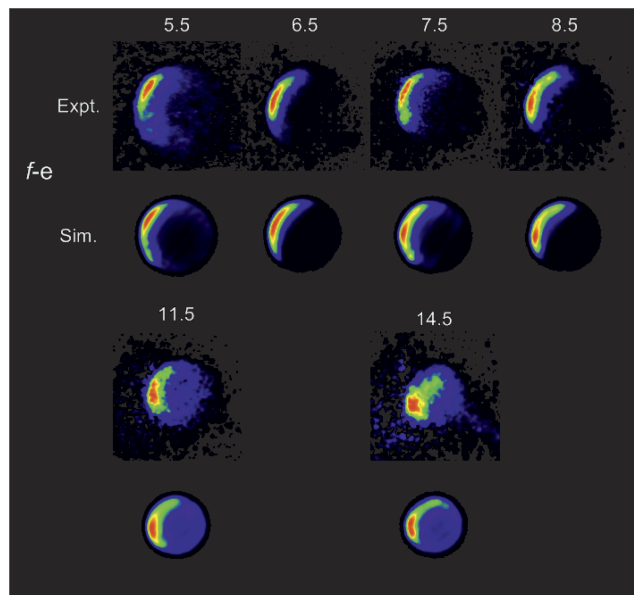


FIG. 7. Ion images for the inelastic scattering of NO + O<sub>2</sub> in the spin-orbit conserving manifold for the final  $e$   $\Lambda$ -doublet ( $\Lambda$ -doublet changing) states of NO, with  $j'_{\text{NO}}$  rotational states as indicated. The experimental images are shown on the top row, with the back-simulations, calculated as described in Sec. III C from the extracted DCSs on the bottom row, together with the determined O<sub>2</sub> rotational population.

each case, the back-simulated image is the result of simulation of each oxygen state with the derived DCS, summed across all O<sub>2</sub> states, weighted by the relative population. Apart from the inherent noise in the experimental images, the agreement between the back-simulation and the original image is reasonably good. This suggests that the extracted DCSs reproduce the angular distribution of the scattering for this system as well as the relative population of the  $N'_{\text{O}_2}$  states for each specified NO quantum state. However, some of the more detailed structure is not observed in the final back-simulation, showing the limitations of the onion-peeling method in extracting

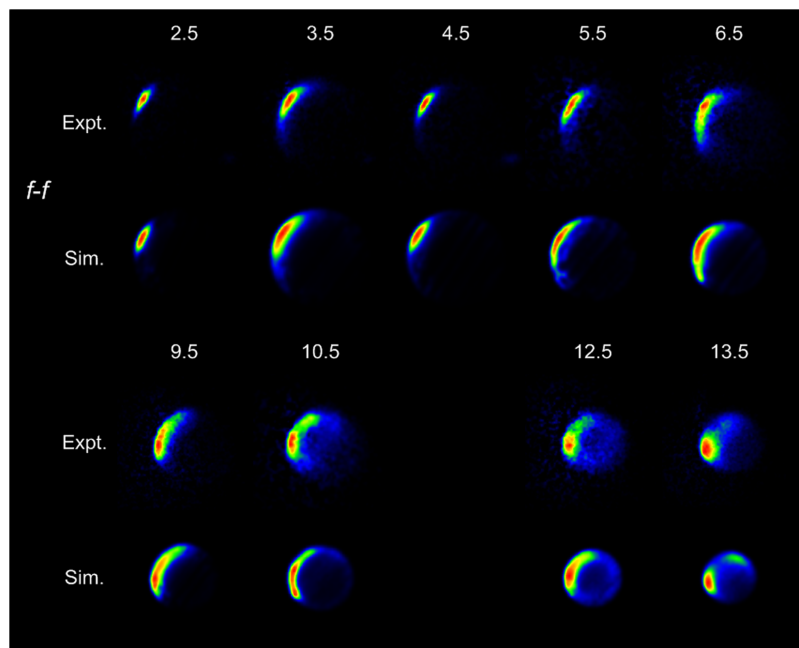


FIG. 6. Ion images for the inelastic scattering of NO + O<sub>2</sub> in the spin-orbit conserving manifold for the final  $f$   $\Lambda$ -doublet ( $\Lambda$ -doublet conserving) states of NO, with  $j'_{\text{NO}}$  rotational states as indicated. The experimental images are shown on the top row, with the back-simulations, calculated as described in Sec. III C from the extracted DCSs on the bottom row, together with the determined O<sub>2</sub> rotational population.



fine details and the limited resolution of the experimental data (we estimate that the angular resolution of the current experiments is between  $10^\circ$  and  $20^\circ$ ). In general, lower  $j'_{\text{NO}}$  states are reproduced better by this method than higher rotational states, due to the lower level of noise in the former experimental ion images.

The ion images show increasingly backward scattered intensity as the rotational state of NO increases, similar to that observed in the collision of NO with the rare gases.<sup>7,62</sup> This occurs because more head-on collisions, leading to scattering through larger angles, are required to populate higher  $j'_{\text{NO}}$  values. The ion images and returned DCSs tend to be dominated by the presence of a single peak in the angular distribution and show little evidence of secondary maxima, which are typically associated with collisions of NO with the rare gases.<sup>13,62</sup> This may in part be due to the overlap of features in the ion images due to the contributions from the multiple oxygen quantum states within the image.

Figure 8 shows the angular scattering distributions for spin-orbit conserving transitions into the final states,  $j'_{\text{NO}} = 4.5f$ ,  $7.5e$ , and  $13.5f$ , resolved into the final oxygen rotational state,  $N'_{\text{O}_2}$ . The DCSs are presented such that the oxygen rotational state increases from the front to the back of the

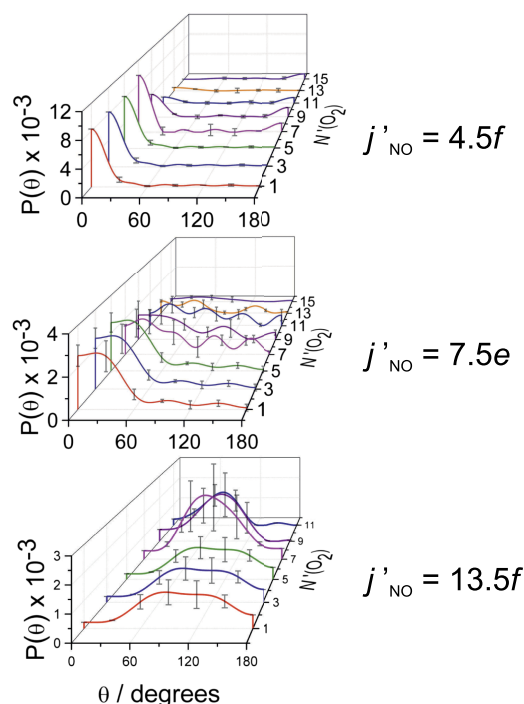


FIG. 8. Angular distributions (relative DCSs) for the inelastic scattering of NO + O<sub>2</sub>, fully resolved in final rotational state of NO,  $j'_{\text{NO}} = 4.5f$  (top),  $7.5e$  (middle), and  $13.5f$  (bottom), and partially resolved in that of O<sub>2</sub>,  $N'_{\text{O}_2}$ . The final oxygen rotational states range from the ground state ( $N'_{\text{O}_2} = 1$ ), at the front, to the maximally energetically allowed state,  $N'_{\text{max(O}_2)}$ , at the back. Note that the three plots are scaled arbitrarily with respect to each other, but that within each panel, the oxygen DCSs are representative of the relative cross section of the final O<sub>2</sub> state population. Note that the experiments cannot resolve the separate angular distributions for  $N'_{\text{O}_2} = 1-5$ , and so the angular distributions for these three O<sub>2</sub> states are attributed the same angular distribution and intensity. DCSs are fitted using a Legendre polynomial expansion including up to the 8th order polynomial. Error bars are calculated by considering the standard error for the fast and slow sides of the ion image combined with the error in changing the Newton sphere radii by  $\pm 1$  pixel.

plot. Bear in mind that for  $N'_{\text{O}_2} = 1-5$  only the average DCS is returned with confidence in the onion-peeling process because of the blurring from the velocity spreads of the molecular beams. Each DCS within a plot is weighted to the relative contribution of the oxygen product rotational state; however, no information about the  $j'_{\text{NO}}$  dependence of the relative integral cross sections is available from the current experiment, and therefore the scales for each  $j'_{\text{NO}}$  are arbitrary.

Large differences between low, middle, and high  $j'_{\text{NO}}$  may be observed in this series of plots. First, the DCSs become overall more backwards scattered as  $j'_{\text{NO}}$  is increased, as already noted above and previously observed for the scattering of NO with O<sub>2</sub> in the study by Bacon *et al.*<sup>30</sup> Second, for increasing  $N'_{\text{O}_2}$ , the angular distributions also become peaked more to the sideways and backwards directions. This may be explained in a manner equivalent to that described for the NO molecule. When the collision partner is a diatom, both partners may be rotationally excited. If the collision is more head-on, both diatoms will have a similar response, with large amounts of translational energy being transferred into rotational energy of both fragments and both products being scattered in a more backward direction. Higher rotational excitation in both scattered products requires more impulsive, head-on collisions.

The rotational dependence of the scattering dynamics of the NO and O<sub>2</sub> molecules can be understood qualitatively by considering the difference between head-on and glancing collisions. Glancing collisions, occurring preferentially at high impact parameters and correlating with low scattering angles, give rise to very little rotational excitation. Therefore, for  $j'_{\text{NO}} = 2.5f$ , whilst there is enough energy in the collision to allow for high oxygen rotation, the glancing nature of the collision does not provide sufficient torque for the population of  $N'_{\text{O}_2} > 9$ , whose population is consequently very low. When the collision takes place by more head-on, low impact parameter collisions, leading to scattering into large angles, such as for the NO  $j'_{\text{NO}} = 14.5e$  rotational state, the rotational excitation of the O<sub>2</sub> collision partner is also large, and the highest  $N'_{\text{O}_2}$  levels are populated.  $j'_{\text{NO}} = 7.5e$  is an intermediate case, in which enough energy is available to allow partitioning of energy into many oxygen states. More head-on collisions give rise to the sideways and backwards scattering observed at middle and high  $N'_{\text{O}_2}$ , and glancing collisions give the forwards scattering at low  $N'_{\text{O}_2}$ .

The average DCS for a specific final NO rotational state is the weighted sum of the fully state-resolved DCSs shown in Fig. 8 over all final populated oxygen rotational states,  $N'_{\text{O}_2}$ , showing the preferential angles of scattering as a function of  $j'_{\text{NO}}$  only. Figures 9 and 10 show the average DCSs for scattering into all experimentally measured NO  $f$  and  $e$  final rotational states, for spin-orbit conserving transitions to the NO  $\Omega' = 0.5$  spin-orbit manifold. The experimentally recovered DCS has an arbitrary intensity based on the intensity of the experimental image, and therefore normalized angular distributions are plotted here. The trends observed in the average DCSs confirm the conclusions drawn from the experimental ion images. Forward scattering is predominant for the lowest  $j'_{\text{NO}}$  states, with increasing sideways and backwards scattering observed for higher  $j'_{\text{NO}}$ . These average DCSs indicate that secondary

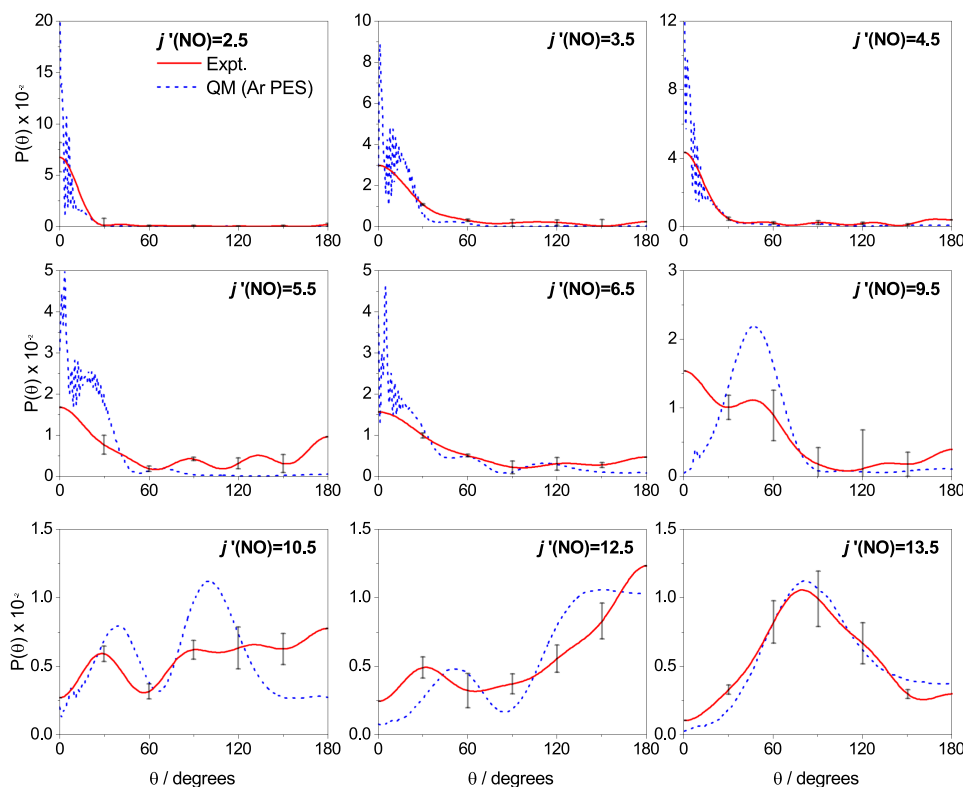


FIG. 9.  $O_2$  state-summed, normalized angular distributions for scattering into final  $f$   $\Lambda$ -doublet states of NO within the spin-orbit conserving manifold. For the experimental data (red continuous line), the angular distributions are summed over all of the populated  $N'O_2$  states at each scattering angle. Error bars are calculated by propagating the errors described in Fig. 8. QM calculations (blue dashed line) show the angular distribution for a “spherical” (atom-like)  $O_2$  molecule colliding with NO on the NO + Ar PES. The QM data have been averaged over the experimental collision energy distribution.

DCS maxima tend not to be observed, since a single peak usually dominates the  $O_2$  state-averaged DCSs.

Figures 9 and 10 also compare the experimentally derived angular distributions with those obtained from CC QM calculations, treating the  $O_2$  collision partner as if it were a closed-shell atom. As noted in Sec. III B, these calculations were performed on the NO + Ar PESs,<sup>1,2</sup> but replacing the mass of Ar by that of  $O_2$ . Given the approximate nature of the theory, the agreement between the experimental data and the QM calculations is not expected to be good, but the two data sets do display a similar qualitative behavior; the QM calculations largely reproduce the general structure seen in the experimental angular distributions. This seems to suggest that the PESs for Ar and  $O_2$  are quite similar and that spin-coupling effects

(due to the radical nature of the  $O_2$  molecule) have only a relatively small effect on the  $N'O_2$  averaged angular distribution. Of course, the true diatomic nature of the  $O_2$  molecule would also have to be considered to extract the fully resolved  $N'O_2, j'_{NO}$  correlated angular distributions. A more subtle feature of the experimental and calculated angular distributions compared in Figs. 9 and 10 is that whilst the QM calculated angular distributions frequently show significant secondary peaks, such secondary features are not seen so clearly in the case of scattering  $O_2$ . Unlike the QM DCSs, which model the scattering as if  $O_2$  were a structureless atom,<sup>7,62</sup> those for NO +  $O_2$  show little evidence of a secondary structure. It is possible that in the case of scattering with  $O_2$  such a structure is only present in low states, which would not be resolved given the overlap

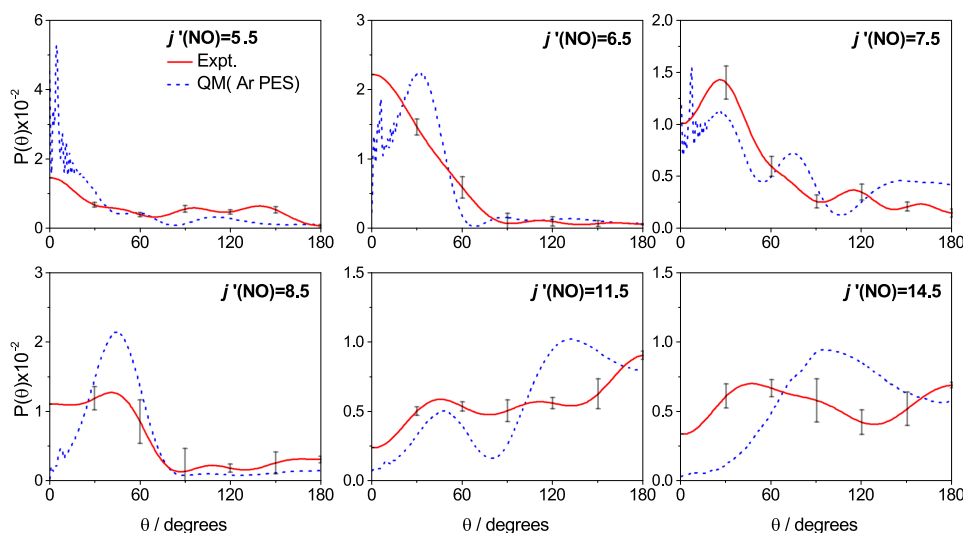


FIG. 10.  $O_2$  state-summed, normalized angular distributions for scattering into final  $e$   $\Lambda$ -doublet states of NO within the spin-orbit conserving manifold. For the experimental data (red continuous line), the angular distributions are summed over all of the populated  $N'O_2$  states at each scattering angle. Error bars are calculated by propagating the errors described in Fig. 8. QM calculations (blue dashed line) show the angular distribution for a “spherical” (atom-like)  $O_2$  molecule colliding with NO on the NO + Ar PES. The QM data have been averaged over the experimental collision energy distribution.

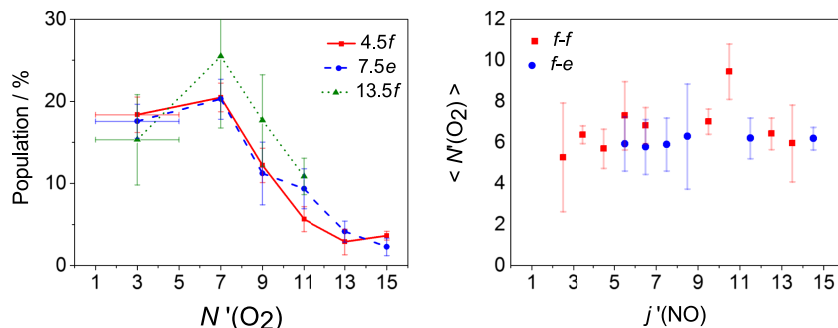


FIG. 11. Effect of  $j'_{NO}$  on  $N'_{O_2}$ : the left panel shows the relative percentage population in each  $N'_{O_2}$  for specific NO rotational states ( $j'_{NO} = 4.5f, 7.5e, 13.5f$  shown with red, blue, and green lines, respectively). Error bars are calculated by considering the population of states for the fast and slow sides of the image and ring radii of  $\pm 1$  pixel. The right panel shows the average oxygen rotational state,  $\langle N'_{O_2} \rangle$ , for both the final  $f$  (red squares) and  $e$  (blue circles) states.  $\langle N'_{O_2} \rangle$  is calculated according to Eq. (4), with error bars calculated from the different population as described for the left panel.

of oxygen in levels  $N'_{O_2} = 1, 3$ , and  $5$ . Since the four PESs describing the scattering of  $NO + O_2$  might be expected to be accessed approximately according to their spin degeneracy, the scattering on the quartet surface (which is predicted to be repulsive in nature) may be expected to be more important than the scattering on the doublet surface, which may account for the lack of the secondary structure observed.

Previous work on the inelastic scattering of NO with the rare gases has revealed the presence of so-called “parity pairs,” in which the DCSs of pairs of states with a common value of  $n = j' - \epsilon\epsilon'/2$  display very similar DCSs.<sup>6,7,22,62,63,67</sup> The origin of this behavior has been shown to lie in the fact that the parity pair transitions are coupled by the same terms in the interaction potential.<sup>22,67</sup> It is interesting to know if a similar behavior is seen in the more complex  $NO + O_2$  system studied here. A comparison of the angular distributions for transitions to the  $f$   $\Lambda$ -doublet levels of  $j' = 6.5, 9.5$ , and  $12.5$  (see Fig. 9) with those for transitions to the  $e$  levels of  $j' = 5.5, 8.5$ , and  $11.5$  (see Fig. 10) suggests that similar parity pair effects are present in the  $NO + O_2$  system, at least as far as the data averaged over the  $O_2$  rotational quantum state. It will be of interest to see whether these effects are also seen in  $O_2$  quantum state-resolved data, but this will require measurements with higher resolution than those currently possible with the current molecular beam instrument.

Since all the oxygen rotational states (for a specific  $j'_{NO}$ ) are extracted from a single ion image using an onion-peeling methodology, information about the relative population with which these states are formed is also obtained. The population of each state is contained inherently within the DCS extracted from the experimental image; the integral of the DCS over all angles therefore gives a relative measure of the relative cross section for that  $O_2$  co-partner quantum state. Thus the relative cross section of each  $N'_{O_2}$  state for final  $j'_{NO}$  may be determined. Note that at the collision energy of the experiment, the maximum populated  $O_2$  rotational quantum state is constrained by energy conservation to  $N'_{O_2} = 19$  and  $1$  for  $\Delta j_{NO} = 1$  and  $17$ , respectively. The left panel of Fig. 11 shows the relative population of states for several  $j'_{NO}$  in the low, middle, and high rotational regimes. The form of the population curve is similar for all  $j'_{NO}$  observed, with a peak population at mid- $N'_{O_2}$ . The lowest  $O_2$  final rotational states ( $N'_{O_2} = 1, 3$ , and  $5$ ) have been assigned the same population (as represented in the figure by a

single point associated with  $N'_{O_2} = 3$ , with error bars), since the first three rotational states are too close in energy to distinguish within the resolution of the experiment. As the rotational excitation of the NO molecule increases, the population of  $O_2$  in higher rotational states increases somewhat with a corresponding decrease in the population of the lowest energy rotational states.

The average final rotational state of molecular oxygen, in pairwise correlation with a given detected NO quantum state, may be calculated according to

$$\langle N'_{O_2} \rangle = \sum_{N'_{O_2}}^{N'_{\max(O_2)}} P(N'_{O_2}) N'_{O_2}, \quad (4)$$

where  $P(N'_{O_2})$  is the normalized population distribution over oxygen rotational states of interest. The average oxygen state, shown for all states in the right panel of Fig. 11, is found to increase very modestly with increasing  $j'_{NO}$  rotational state, within the errors of the data. (The Pearson correlation coefficient for the dependence of  $\langle N'_{O_2} \rangle$  on  $j'_{NO}$  was calculated to be  $0.47$  and  $0.87$  for the  $f-f$  and  $f-e$  transitions, respectively, showing a statistically significant positive correlation.) This shows that higher oxygen rotational states may be populated somewhat more readily when the NO molecule is also excited into high rotational states, as observed for the  $N'_{O_2}$ -resolved DCSs. The exhibited trend can be understood by considering the DCSs for different  $N'_{O_2}$  but the same  $j'_{NO}$ . As  $N'_{O_2}$  increases, the DCS becomes more back-scattered, due to more head-on collisions required for higher rotational excitation. As we have already noted, these head-on type collisions are likely to induce large amounts of rotational excitation in both the NO molecule and the  $O_2$  collision partner. This means that higher values of  $j'_{NO}$  correlate somewhat with higher values of  $N'_{O_2}$ . Hence, as  $j'_{NO}$  increases, the population in the higher  $N'_{O_2}$  states will also increase, as these states become preferentially populated by head-on collisions, and the average value of the oxygen rotational state will also increase.

## V. CONCLUSIONS AND OUTLOOK

We have presented an experimental study of the inelastic scattering of fully quantum state-resolved NO with  $O_2$

using hexapole state-selection, coupled with velocity-map ion imaging. A methodology based on the onion-peeling algorithm is presented for the extraction of the  $N'_{O_2}$ -resolved DCSs and their relative  $N'_{O_2}$  population. The DCSs and population for spin-orbit conserving transitions to both the  $f$  and  $e$  final  $\Lambda$ -doublet states of NO have been shown to provide useful information on the detailed dynamics of inelastic processes. The relative population distribution along with the angular distributions of sequential oxygen rotational states can be used to understand the scattering behavior of the NO–O<sub>2</sub> system. There is a trade-off at a given collision energy between the partitioning of rotational energy transferred to the two diatoms along with the oxygen rotational states, which are energetically accessible within each  $j'_{NO}$ . Both NO and O<sub>2</sub> show increasingly backward scattering as their rotational state is increased, since collisions that induce large rotational excitation in the NO molecule are also likely to induce rotational excitation in O<sub>2</sub>. However, further work is required to fully understand the effects of rotational excitation in diatom-diatom collisions. The collisions between NO and Ar and O<sub>2</sub> collision partners have been shown to be quite similar in nature. The major difference between the scatterings of the collision partners are the lack of obvious secondary maxima observed for scattering by O<sub>2</sub>. Further theoretical work is required to understand the lack of such features in the scattering distribution. However, this is impeded by the lack of high-quality PESs for the NO + O<sub>2</sub> systems and the complexity of scattering dynamics, which, in principle, could involve coupled motion on four coupled PESs.

Current improvements to the experimental apparatus include the implementation of new slicing apparatus, utilising the PImMS sensor.<sup>54</sup> This slicing technique will allow the three-dimensional Newton sphere to be obtained for diatom-diatom scattering with increased resolution.<sup>55</sup> By reconstructing the three-dimensional sphere (from the slices extracted during ion imaging), it may be possible to directly isolate the nested Newton spheres, allowing them to be analysed without interference from other excited oxygen states. This will allow DCSs and polarization effects to be obtained and analysed as a function of the O<sub>2</sub> final rotational state, thus allowing easier separation of the state dependent contributions than that presented here for oxygen as the collision partner. A further improvement would be to control more precisely the collision energy distribution through the use of a Stark decelerator.<sup>14–16</sup> Such improvements are probably essential to obtaining fully quantum state-resolved pair-correlated DCSs in this and other similar diatom-diatom systems.

## ACKNOWLEDGMENTS

The support of the UK EPSRC (to M.B. via Programme Grant No. EP/L005913/1) and the EU (to M.B. via FP7 EU People ITN Project No. 238671) is acknowledged. F.J.A. acknowledges funding from the Spanish Ministry of Economy and Competitiveness (Grant Nos. CSD2009-00038 and MINECO CTQ2015-65033-P), and S.S. acknowledges support from the National Basic Research Program of China (973 program) under Grant No. 2013CB922200 and from the National Science Foundation of China under Grant Nos.

11034003 and 91221301. S.D.S.G. and M.B. also thank Cambio, Ltd., and Dr. Peter Dean for generous support.

- <sup>1</sup>M. H. Alexander, *J. Chem. Phys.* **111**, 7426 (1999).
- <sup>2</sup>M. H. Alexander, *J. Chem. Phys.* **111**, 7435 (1999).
- <sup>3</sup>M. S. Elioff and D. W. Chandler, *J. Chem. Phys.* **117**, 6455 (2002).
- <sup>4</sup>F. J. Aoiz, J. E. Verdasco, V. J. Herrero, V. Saez Rabanos, and M. H. Alexander, *J. Chem. Phys.* **119**, 5860 (2003).
- <sup>5</sup>E. A. Wade, K. Thomas Lorenz, D. W. Chandler, J. W. Barr, G. L. Barnes, and J. I. Cline, *Chem. Phys.* **301**, 261 (2004).
- <sup>6</sup>A. Gijsbertsen, H. Linnartz, G. Rus, A. E. Wiskerke, S. Stolte, D. W. Chandler, and J. Klos, *J. Chem. Phys.* **123**, 224305 (2005).
- <sup>7</sup>C. J. Eyles, M. Brouard, C.-H. Yang, J. Klos, F. J. Aoiz, A. Gijsbertsen, A. E. Wiskerke, and S. Stolte, *Nat. Chem.* **3**, 597 (2011).
- <sup>8</sup>J. Klos, F. J. Aoiz, M. Menéndez, M. Brouard, H. Chadwick, and C. J. Eyles, *J. Chem. Phys.* **137**, 014312 (2012).
- <sup>9</sup>M. Brouard, H. Chadwick, C. J. Eyles, B. Hornung, B. Nichols, F. J. Aoiz, P. G. Jambrina, and S. Stolte, *J. Chem. Phys.* **138**, 104310 (2013).
- <sup>10</sup>M. Brouard, H. Chadwick, C. J. Eyles, B. Hornung, B. Nichols, F. J. Aoiz, P. G. Jambrina, S. Stolte, and M. P. de Miranda, *J. Chem. Phys.* **138**, 104309 (2013).
- <sup>11</sup>M. Brouard, H. Chadwick, C. J. Eyles, B. Hornung, B. Nichols, J. M. Scott, F. J. Aoiz, J. Klos, S. Stolte, and X. Zhang, *Mol. Phys.* **111**, 1759 (2013).
- <sup>12</sup>M. Brouard, H. Chadwick, S. D. S. Gordon, B. Hornung, B. Nichols, J. Klos, F. J. Aoiz, and S. Stolte, *J. Chem. Phys.* **141**, 164306 (2014).
- <sup>13</sup>H. Chadwick, B. Nichols, S. D. S. Gordon, B. Hornung, E. Squires, M. Brouard, J. Klos, M. H. Alexander, F. J. Aoiz, and S. Stolte, *J. Phys. Chem. Lett.* **5**, 3296 (2014).
- <sup>14</sup>A. von Zastrow, J. Onvlee, S. N. Vogels, G. C. Groenenboom, A. van der Avoird, and S. Y. T. van de Meerakker, *Nat. Chem.* **6**, 216 (2014).
- <sup>15</sup>S. N. Vogels, J. Onvlee, A. von Zastrow, G. C. Groenenboom, A. van der Avoird, and S. Y. T. van de Meerakker, *Phys. Rev. Lett.* **113**, 263202 (2014).
- <sup>16</sup>J. Onvlee, S. N. Vogels, A. van der Avoird, G. C. Groenenboom, and S. Y. T. van de Meerakker, *New J. Phys.* **17**, 055019 (2015).
- <sup>17</sup>M. T. Vonk, J. A. Bacon, C. F. Giese, and W. R. Gentry, *J. Chem. Phys.* **106**, 1353 (1997).
- <sup>18</sup>M. J. L. de Lange, M. Drabbels, P. T. Griffiths, J. Bulthuis, S. Stolte, and J. G. Snijders, *Chem. Phys. Lett.* **313**, 491 (1999).
- <sup>19</sup>M. H. Alexander, *Faraday Discuss.* **113**, 437 (1999).
- <sup>20</sup>H. Kohguchi, T. Suzuki, and M. H. Alexander, *Science* **294**, 832 (2001).
- <sup>21</sup>K. T. Lorenz, D. W. Chandler, J. W. Barr, W. Chen, G. L. Barnes, and J. I. Cline, *Science* **293**, 2063 (2001).
- <sup>22</sup>A. Gijsbertsen, H. Linnartz, C. A. Taatjes, and S. Stolte, *J. Am. Chem. Soc.* **128**, 8777 (2006).
- <sup>23</sup>S. Marinakis, B. J. Howard, F. J. Aoiz, and J. Klos, *Chem. Phys. Lett.* **512**, 161 (2011).
- <sup>24</sup>B. Nichols, H. Chadwick, S. D. S. Gordon, C. J. Eyles, B. Hornung, M. Brouard, M. H. Alexander, F. J. Aoiz, A. Gijsbertsen, and S. Stolte, *Chem. Sci.* **6**, 2202 (2015).
- <sup>25</sup>A. Khachatryan and P. J. Dagdigian, *J. Phys. Chem. A* **113**, 13390 (2009).
- <sup>26</sup>S. Chefderville, Y. Kalugina, S. Y. T. van de Meerakker, C. Naulin, F. Lique, and M. Costes, *Science* **341**, 1094 (2013).
- <sup>27</sup>M. Kirste, X. Wang, H. C. Schewe, G. Meijer, K. Liu, A. van der Avoird, L. M. C. Janssen, K. B. Gubbels, G. C. Groenenboom, and S. Y. T. van de Meerakker, *Science* **338**, 1060 (2012).
- <sup>28</sup>A. Moise, R. Cireasa, D. H. Parker, and J. J. ter Meulen, *J. Chem. Phys.* **125**, 204315 (2006).
- <sup>29</sup>A. Moise, D. H. Parker, and J. J. ter Meulen, *J. Chem. Phys.* **126**, 124302 (2007).
- <sup>30</sup>J. A. Bacon, C. F. Giese, and W. R. Gentry, *J. Chem. Phys.* **108**, 3127 (1998).
- <sup>31</sup>C. R. Bieler, A. Sanov, and H. Reisler, *Chem. Phys. Lett.* **235**, 175 (1995).
- <sup>32</sup>A. T. J. B. Eppink and D. H. Parker, *Rev. Sci. Instrum.* **68**, 3477 (1997).
- <sup>33</sup>D. W. Chandler and P. L. Houston, *J. Chem. Phys.* **87**, 1445 (1987).
- <sup>34</sup>C. Bordas, F. Paulig, H. Helm, and D. L. Huestis, *Rev. Sci. Instrum.* **67**, 2257 (1996).
- <sup>35</sup>T. Peter Rakitzis, *Chem. Phys. Lett.* **342**, 121 (2001).
- <sup>36</sup>V. Dribinski, A. Ossadtchi, V. A. Mandelshtam, and H. Reisler, *Rev. Sci. Instrum.* **73**, 2634 (2002).
- <sup>37</sup>G. A. Garcia, L. Nahon, and I. Powis, *Rev. Sci. Instrum.* **75**, 4989 (2004).
- <sup>38</sup>M. I. Apostolopoulos, M. I. Taroudakis, and D. G. Papazoglou, *Opt. Commun.* **296**, 25 (2013).
- <sup>39</sup>S. Manzhos and H.-P. Loock, *Comput. Phys. Commun.* **154**, 76 (2003).
- <sup>40</sup>G. M. Roberts, J. L. Nixon, J. Lecomte, E. Wrede, and J. R. R. Verlet, *Rev. Sci. Instrum.* **80**, 053104 (2009).



- <sup>41</sup>V. K. Nestorov, R. D. Hinchliffe, R. Uberna, J. I. Cline, K. T. Lorenz, and D. W. Chandler, *J. Chem. Phys.* **115**, 7881 (2001).
- <sup>42</sup>K. Zhao, T. Colvin, W. T. Hill, and G. Zhang, *Rev. Sci. Instrum.* **73**, 3044 (2002).
- <sup>43</sup>M. J. Bass, M. Brouard, A. P. Clark, and C. Vallance, *J. Chem. Phys.* **117**, 8723 (2002).
- <sup>44</sup>B. Dick, *Phys. Chem. Chem. Phys.* **16**, 570 (2014).
- <sup>45</sup>M. G. González, J. D. Rodríguez, L. Rubio-Lago, and L. Bañares, *Phys. Chem. Chem. Phys.* **16**, 26330 (2014).
- <sup>46</sup>C. R. Gebhardt, T. P. Rakitzis, P. C. Samartzis, V. Ladopoulos, and T. N. Kitsopoulos, *Rev. Sci. Instrum.* **72**, 3848 (2001).
- <sup>47</sup>T. P. Rakitzis and T. N. Kitsopoulos, *J. Chem. Phys.* **116**, 9228 (2002).
- <sup>48</sup>J. J. Lin, J. Zhou, W. Shiu, and K. Liu, *Rev. Sci. Instrum.* **74**, 2495 (2003).
- <sup>49</sup>D. Townsend, M. P. Minitti, and A. G. Suits, *Rev. Sci. Instrum.* **74**, 2530 (2003).
- <sup>50</sup>S.-M. Wu, X. Yang, and D. H. Parker, *Mol. Phys.* **103**, 1797 (2005).
- <sup>51</sup>D. Nandi, V. S. Prabhudesai, E. Krishnakumar, and A. Chatterjee, *Rev. Sci. Instrum.* **76**, 053107 (2005).
- <sup>52</sup>I. Wilkinson and B. J. Whitaker, *J. Chem. Phys.* **129**, 154312 (2008).
- <sup>53</sup>L. Rubio-Lago, J. D. Rodríguez, A. García-Vela, M. G. González, G. A. Amaral, and L. Bañares, *Phys. Chem. Chem. Phys.* **13**, 8186 (2011).
- <sup>54</sup>C. Vallance, M. Brouard, A. Lauer, C. S. Slater, E. Halford, B. Winter, S. J. King, J. W. L. Lee, D. E. Pooley, I. Sedgwick, R. Turchetta, A. Nomerotski, J. J. John, and L. Hill, *Phys. Chem. Chem. Phys.* **16**, 383 (2014).
- <sup>55</sup>K. Amini, S. Blake, M. Brouard, M. B. Burt, E. Halford, A. Lauer, C. S. Slater, J. W. L. Lee, and C. Vallance, *Rev. Sci. Instrum.* **86**, 103113 (2015).
- <sup>56</sup>M. H. Alexander, *J. Chem. Phys.* **76**, 5974 (1982).
- <sup>57</sup>M. H. Alexander, *Chem. Phys.* **92**, 337 (1985).
- <sup>58</sup>E. P. F. Lee and T. G. Wright, *Chem. Phys. Lett.* **347**, 429 (2001).
- <sup>59</sup>P. E. M. Siegbahn, *J. Comput. Chem.* **6**, 182 (1985).
- <sup>60</sup>H. F. Davis, B. Kim, H. S. Johnston, and Y. T. Lee, *J. Phys. Chem.* **97**, 2172 (1993).
- <sup>61</sup>L. Valachovic, C. Riehn, K. Mikhaylichenko, and C. Wittig, *Chem. Phys. Lett.* **258**, 644 (1996).
- <sup>62</sup>C. J. Eyles, M. Brouard, H. Chadwick, B. Hornung, B. Nichols, C.-H. Yang, J. Klos, F. J. Aoiz, A. Gijsbertsen, A. E. Wiskerke, and S. Stolte, *Phys. Chem. Chem. Phys.* **14**, 5403 (2012).
- <sup>63</sup>C. J. Eyles, M. Brouard, H. Chadwick, F. J. Aoiz, J. Klos, A. Gijsbertsen, X. Zhang, and S. Stolte, *Phys. Chem. Chem. Phys.* **14**, 5420 (2012).
- <sup>64</sup>HIBRIDON is a package of programs for the time-independent quantum treatment of inelastic collisions and photodissociation written by M. H. Alexander, D. E. Manolopoulos, H.-J. Werner, and B. Follmeg, with contributions by P. F. Vohralik, D. Lemoine, G. Corey, R. Gordon, B. Johnson, T. Orlikowski, A. Berning, A. D. Esposti, C. Rist, P. Dagdigian, B. Pouilly, G. van der Sanden, M. Yang, F. de Weerd, S. Gregurick, and J. Klos.
- <sup>65</sup>C. J. Dasch, *Appl. Opt.* **31**, 1146 (1992).
- <sup>66</sup>M. H. Alexander, *J. Chem. Phys.* **99**, 7725 (1993).
- <sup>67</sup>J. Klos, F. J. Aoiz, J. E. Verdasco, M. Brouard, S. Marinakis, and S. Stolte, *J. Chem. Phys.* **127**, 031102 (2007).